

The evolution of the Si IV content in the Universe from the epoch of reionization to cosmic noon

V. D’Odorico^{1,2,3*}, K. Finlator^{4,5}, S. Cristiani^{1,3}, G. Cupani^{1,3}, S. Perrotta⁶, F. Calura⁷,
M. Cènturion¹, G. Becker⁸, T. A. M. Berg^{9,10}, S. Lopez¹⁰, S. Ellison¹¹, E. Pomante¹

¹ INAF- Osservatorio Astronomico di Trieste, Via Tiepolo 11, I-34143 Trieste, Italy

² Scuola Normale Superiore di Pisa, Piazza dei Cavalieri 7, I-56126 Pisa, Italy

³ IFPU–Institute for Fundamental Physics of the Universe, via Beirut 2, I-34151 Trieste, Italy

⁴ New Mexico State University, Las Cruces, NM, USA

⁵ Cosmic Dawn Center (DAWN), Niels Bohr Institute, University of Copenhagen / DTU-Space, Technical University of Denmark

⁶ Department of Astronomy, University of California, San Diego, CA 92092, USA

⁷ INAF - Osservatorio Astronomico di Bologna, Via Ranzani 1, 40127 Bologna, Italy

⁸ Department of Physics & Astronomy, University of California, Riverside, CA 92521, USA

⁹ ESO - European Southern Observatory, Alonso de Cordova 3107, Casilla 19001, Santiago, Chile

¹⁰ Departamento de Astronomía, Universidad de Chile, Casilla 36-D, Santiago, Chile

¹¹ Department of Physics & Astronomy, University of Victoria, Finnerty Road, Victoria, British Columbia V8P 1A1, Canada

Accepted XXX. Received YYY; in original form ZZZ

ABSTRACT

We investigate the abundance and distribution of metals in the high-redshift intergalactic medium and circum-galactic medium through the analysis of a sample of almost 600 Si IV absorption lines detected in high and intermediate resolution spectra of 147 quasars. The evolution of the number density of Si IV lines, the column density distribution function and the cosmic mass density are studied in the redshift interval $1.7 \lesssim z \lesssim 6.2$ and for $\log N(\text{Si IV}) \geq 12.5$. All quantities show a rapid increase between $z \sim 6$ and $z \lesssim 5$ and then an almost constant behaviour to $z \sim 2$ in very good agreement with what is already observed for C IV absorption lines. The present results are challenging for numerical simulations: when simulations reproduce our Si IV results, they tend to underpredict the properties of C IV, and when the properties of C IV are reproduced, the number of strong Si IV lines ($\log N(\text{Si IV}) > 14$) is overpredicted.

Key words: intergalactic medium, quasars: absorption lines, cosmology: observations, reionization, galaxies:high-redshift

1 INTRODUCTION

Galaxies evolve through continuous exchanges of gas with the surrounding circumgalactic medium (CGM) and intergalactic medium (IGM). In the scenario suggested by state-of-the-art simulations, galaxies at the cosmic noon ($z \sim 2 - 3$) accrete a substantial fraction of their gas through “cold flows”, dense filamentary accretion streams that flow nearly unaffected through the galaxy halo and provide cold, $T \sim 10^4$ K, gas accretion to the interstellar medium (ISM; e.g. [Birnboim & Dekel 2003](#); [Kereš et al. 2005](#); [Faucher-Giguère, Kereš, & Ma 2011](#); [van de Voort et al. 2011](#); [Nelson et al. 2013](#); [Theuns 2021](#)). At the same time, the vigorous star formation activity going on in these high- z galaxies favours the dispersion in the CGM (and eventually, IGM) of the metal enriched gas through feedback mechanisms driven by galactic winds, SN explosions and accretion onto black holes (e.g. [Madau, Ferrara, & Rees 2001](#); [Calura & Matteucci 2006](#); [Barai et al.](#)

[2013](#); [Suresh et al. 2015](#); [Turner et al. 2016](#); [Muratov et al. 2017](#); [Fossati et al. 2021](#)).

While the observational evidence of inflowing cold flows is still tentative (e.g. [Rubin et al. 2012](#)), the presence of metal enriched gas outside galaxies has been well established observationally for more than two decades (e.g. [Cowie et al. 1995](#); [Tytler et al. 1995](#); [Ellison et al. 2000](#); [Schaye et al. 2003](#); [D’Odorico et al. 2016](#)).

The physical properties and chemical composition of the diffuse gas are probed by absorption-line spectroscopy of bright background sources. In particular, metal absorption lines associated with H I Lyman- α ($\text{Ly}\alpha$) clouds with column densities $\log N(\text{H I}) \lesssim 17.3$ are thought to arise in gas located on the outskirts of galaxies and further away, in the shallow IGM, as the H I column density decreases ([van de Voort et al. 2012](#)).

Several studies have investigated the properties of metals close to galaxies by considering the correlation between the metal absorptions observed along a quasar line of sight and the galaxies present in the field at matching redshifts. All the studies carried out up to now both at high (e.g. [Adelberger et](#)

* E-mail:valentina.dodorico@inaf.it

al. 2005; Steidel et al. 2010; Turner et al. 2014; Lofthouse et al. 2020; Rudie et al. 2019) and low redshift (e.g. Tumlinson et al. 2011; Prochaska et al. 2011; Werk et al. 2014; Liang & Chen 2014; Bordoloi et al. 2014; Johnson et al. 2017; Fossati et al. 2019) agree on the significant presence of metals in high and low ionization state at impact parameters at least as large as $\approx 100 - 300$ kpc. The standard way to carry out this kind of investigation has been by considering samples of galaxy-absorber pairs and deducing the metal distribution in the CGM from a statistical point of view. With the advent of the 30-40m class telescopes (e.g. the ESO Extremely Large Telescope¹), it will be possible to use much fainter sources as background targets for spectroscopy (in particular, galaxies themselves) and pierce the gas surrounding the same galaxy with multiple, close lines of sight to carry out a tomographic study of the CGM. The few examples available today reveal the power of this technique to assess the gas patchiness and its covering factor around individual systems (e.g. López et al. 2018, 2020).

The distribution of metals and the enrichment mechanism at high redshift can be investigated also with large samples of absorption lines detected along many, independent lines of sight to bright sources. The statistical properties derived from those samples can then be compared with model predictions to constrain in particular the adopted feedback mechanisms (e.g. Tescari et al. 2011). The most studied ionic transition at high redshift is the triply ionized carbon doublet (C IV $\lambda\lambda$ 1548, 1551 Å) mainly due to the fact that: *i*) it is commonly observed; *ii*) it falls outside the Ly α forest; *iii*) it is easy to identify thanks to its doublet nature; *iv*) it is observable with ground-based telescopes from $z \simeq 1.0$ to the highest redshift at which we can observe quasars to date. C IV traces ionized gas mostly in the CGM and IGM environment (see e.g. Oppenheimer & Davé 2006; Cen & Chisari 2011; Mongardi et al. 2018). The C IV number density, column density distribution function and cosmic mass density, Ω_{CIV} , are the statistical indicators mostly used to assess the evolution of the abundance of this ion across the history of the Universe (e.g. Scannapieco et al. 2006; Ryan-Weber et al. 2009; Cooksey et al. 2010; D’Odorico et al. 2010; Simcoe et al. 2011; Cooksey et al. 2013; D’Odorico et al. 2013; Codoreanu et al. 2018; Meyer et al. 2019; Cooper et al. 2019; Hasan et al. 2020). Cosmological hydro-dynamical simulations by several groups have tried to reproduce the measured observables (mainly the column density distribution function and the cosmic mass density) all with poor results, in particular for $z \gtrsim 5$ (e.g. Rahmati et al. 2016; Keating et al. 2016). The introduction of a fluctuating ultra-violet background (UVB) improves the agreement but does not solve the problem (Finlator et al. 2018, and references therein). On the other hand, García et al. (2017) are able to reproduce the column density distribution function of C IV at $z \geq 4.35$, but at the price of an overproduction of Si IV. This overabundance of high column density Si IV absorbers is not present in Rahmati et al. (2016) and Finlator et al. (2018).

There are clear numerical limitations in the realization of the optimal C IV simulation: it should both reproduce enough strong absorbers (need of a large box) and a self consistent, inhomogeneous UVB, implementing radiative transfer (com-

putationally very expensive). In addition to the uncertainties in stellar yields and feedback mechanisms, the amount of C IV is made even more difficult to determine by the fact that the ionization potentials to convert C III into C IV and C IV into C V are on the opposite sides of the UVB jump due to the ionization of He II, at 4 Ryd or 54.4 eV. The shape of the UVB at energies > 4 Ryd is very uncertain (see e.g. Fig. 9 in Finlator et al. 2018).

Another tracer of the ionized diffuse gas in the CGM is the triply ionized silicon (Si IV $\lambda\lambda$ 1394, 1403 Å, see e.g. Steidel et al. 2010; Turner et al. 2014; Mongardi et al. 2018), which is not as common as C IV but it shares with the latter the advantage of being a doublet that is observable outside the Ly α forest. Si IV is probably tracing slightly denser gas with respect to C IV, and thus possibly closer to galaxies (e.g. Mongardi et al. 2018). However, among the absorption lines routinely detected in quasar spectra (e.g. C IV, Si IV, O VI, Mg II, Fe II) it is the one that arises from gas in a range of densities and temperatures almost equivalent to those of gas traced by C IV (see e.g. Fig. 12 in Scannapieco et al. 2006). C IV and Si IV are the dominant ionization stages of carbon and silicon in the IGM, and furthermore they are tracers of Fe-coproduction and α -element processes, respectively. Si IV can be observed from the ground for $z \gtrsim 1.15$. A bonus of Si IV with respect to C IV is that the ionization potentials to turn Si III into Si IV and Si IV into Si V fall in the energy range $2 < IP < 4$ Ryd, where the different UVB models behave very similarly.

In her pioneering work, Songaila (2001) analysed both C IV and Si IV absorption lines for a sample of 32 quasars observed with HIRES and ESI at the Keck telescope, covering the redshift range $1.7 \lesssim z \lesssim 5.3$. Considering Si IV lines with column density $12.00 \leq \log N(\text{Si IV}) \leq 14.8$, she found that the cosmic mass density of this ion, Ω_{SiIV} , keeps approximately constant at lower redshift with a downturn at $z > 4.5$ (see Fig. 5). Subsequent works that investigated the properties of Si IV absorbers were all based on smaller samples and/or narrower redshift ranges (e.g. Scannapieco et al. 2006; Cooksey et al. 2011; Shull et al. 2014; Boksenberg & Sargent 2015; Codoreanu et al. 2018). In general, they all confirmed the redshift behaviour of Ω_{SiIV} observed by Songaila (2001). Observationally, Si IV broadly matches the behaviour of C IV in terms of redshift evolution of the cosmic mass density and line number density (e.g. Songaila 2001; Boksenberg & Sargent 2015). Also the clustering properties of Si IV absorption lines along the line of sight are in very good agreement with those of C IV suggesting similar sizes for the ion enriched bubbles (Scannapieco et al. 2006).

For all the reasons explained above and because of the large number of available quasar lines of sight observed at intermediate to high resolution and good signal-to-noise ratio (SNR), we believe it is timely to dedicate a paper to Si IV and its statistical properties. In this work, we present a sample of 519 Si IV absorption lines with column density $\log N(\text{Si IV}) \geq 12.5$ observed along 147 quasar lines of sight and covering a very broad redshift range, $z \simeq 1.75 - 6.24$. Our aim is to study in detail the evolution of this ion, contrasted it with C IV and the recently studied O I (Becker et al. 2019), and provide solid observational results to be compared with simulation predictions to help figuring out the physics of the feedback mechanisms. The detailed study of the Si IV and C IV absorptions arising in the same systems (e.g. the determination and

¹ <https://elt.eso.org>

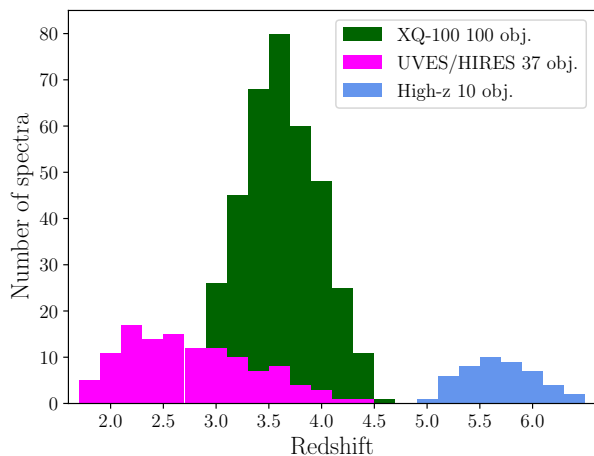


Figure 1. Number of spectra used in this work per redshift bin of $\Delta z = 0.2$.

analysis of the redshift evolution of the Si IV/C IV ratio) will be deferred to a future work.

The paper is organized as follows. Section 2 describes the three spectroscopic samples that have been used in this work. In Section 3, we report the results for the line number density and column density distribution function computed with our sample. Section 4 is devoted to the presentation of the results on the cosmic mass density and its evolution with redshift. In section 5, we compare our results with previous works appeared in the literature. Finally, Section 6 is dedicated to the discussion and conclusions. Throughout this paper, we assume $\Omega_m = 0.3$, $\Omega_\Lambda = 0.7$ and $h \equiv H_0/(100 \text{ km s}^{-1} \text{ Mpc}^{-1}) = 0.70$ if not stated otherwise.

2 DATA SAMPLES AND ANALYSIS

This work is based on three samples of quasar spectra, for a total of 147 lines of sight, which cover different redshift ranges for Si IV absorptions. They are briefly described in the following sections.

In all the considered spectra, Si IV doublets were looked for by eye in the region outside the Ly α forest, redward of the quasar Ly α emission. In case of doubtful detections (e.g. blending of one of the two components of the doublet), we used the presence of a C IV system at the same redshift and with a similar velocity profile to confirm the identification. To avoid contamination from absorption systems associated with the quasars, we considered only absorbers with a maximum redshift, z_{max} , at a separation $\Delta v = -5000 \text{ km s}^{-1}$ from the quasar emission redshift. On the other hand, the contamination from Ly α lines was prevented by taking a minimum redshift, z_{min} , at a separation $\Delta v = +1000 \text{ km s}^{-1}$ from the Ly α emission of the quasar. The considered redshift intervals are reported in Tabs. 1, 2 and 3.

All the detected Si IV absorption lines were fitted with Voigt profiles mainly with the *fitlyman* context of the ESO MIDAS package (Fontana & Ballester 1995). Exceptions are discussed in the sections dedicated to the sample description.

The number of spectra per redshift bin of $\Delta z = 0.2$ for the three samples, is shown in Fig. 1.

2.1 The high-resolution UVES/HIRES sample

This sample collects the high-resolution ($R \simeq 50,000$, $\Delta v \simeq 6.0 \text{ km s}^{-1}$) spectra analysed in D’Odorico et al. (2010) and Calura et al. (2012). For the quasar HE 0940-1050, we used the higher SNR spectrum presented in D’Odorico et al. (2016). Details of the data reduction and analysis are reported in D’Odorico et al. (2010).

Also, we used updated spectra (including new observations) of SDSS J1621-0042 and PKS 1937-101 and added the new spectra of QSO J0407-4410 and QSO J0103+1316. The four new spectra were reduced by E. Pomante in the context of his PhD thesis work², with a custom made pipeline able to ingest both UVES and HIRES raw frames and treat them in the same way. This generalized pipeline is an extension of the IDL code developed by S. Burles and J. X. Prochaska for the reduction of MIKE and HIRES data (Bernstein, Burles, & Prochaska 2015), with a modified approach to wavelength calibration, flat fielding and object extraction.

In order to increase the statistical significance of our sample and the coverage toward higher redshifts, we have considered also the sample of 9 objects analysed in Boksenberg & Sargent (2015, hereafter BS15), which have a similar resolution element of $\Delta v \simeq 6.6 \text{ km s}^{-1}$. For the quasar spectrum of B1422+231, which is in common between our sample and BS15, we considered our list of lines, which is consistent with the BS15 one.

Note that the majority of the quasars in this sample belongs to the UVES Large Programme by Bergeron et al. (2004) which required Lyman- α forests free from Damped Lyman- α systems (DLAs). We have thus verified the presence of DLAs in the additional quasars and excised from the final sample the redshift ranges of the corresponding Si IV lines. In particular, there is a DLA per line of sight in the BS15 spectra of QSO B1425+6039, QSO B1055+4611 and QSO B2237-0607.

The final high-resolution sample is then formed by 37 objects and covers the Si IV redshift range $1.75 \lesssim z \lesssim 4.47$, with a total scanned absorption path of $\Delta X \simeq 54$. In Table 1, we report for each object of the sample the redshift range available for Si IV detection and the SNR per resolution element of 6.6 km s^{-1} at $\lambda_{\text{rest}} \sim 1380 \text{ \AA}$, to be compliant with the SNR reported by BS15. The average SNR ~ 156 corresponds to a 3σ detection threshold for the Si IV $\lambda 1393 \text{ \AA}$ line of $\log N(\text{Si IV})_{\text{thr}} \simeq 11.09$ assuming a conservative $b = 10 \text{ km s}^{-1}$ Doppler parameter. The spectrum with the lowest SNR has $\log N(\text{Si IV})_{\text{thr}} \simeq 11.95$.

BS15 fit absorption lines with the Voigt profile fitting code VPFIT (Carswell et al. 2014). As already shown in previous works (e.g. D’Odorico et al. 2016) there are no significant differences between the results of *fitlyman* and VPFIT. Possible differences due to, for example, an excess of low column density components by VPFIT, are further mitigated by the fact that, as we already did in D’Odorico et al. (2010, 2013), in order to compare these high-resolution spectra with those from XSHOOTER, Si IV lines with velocity separation

² <http://hdl.handle.net/11368/2908079>

Table 1. The high-resolution UVES/HIRES sample. The different columns report: the name of the object, the emission redshift, the minimum and maximum redshift considered for the Si iv absorption lines to be part of the sample, the signal-to-noise ratio per resolution element computed at $\lambda_{\text{rest}} \sim 1380 \text{ \AA}$ and the reference paper.

Object	z_{em}	z_{min}	z_{max}	SNR	Ref.
HE 1341-1020	2.142	1.749	2.090	200	1
QSO B0122-379	2.200	1.801	2.147	114	1
PKS 1448-232	2.224	1.821	2.171	113	1
PKS 0237-230	2.233	1.829	2.179	283	1
HE 0001-2340	2.267	1.859	2.213	190	1
QSO B1626+6426	2.320	1.905	2.265	128	5
HE 1122-1648	2.400	1.975	2.344	314	1
QSO B0109-3518	2.406	1.980	2.349	119	1
HE 2217-2818	2.414	1.988	2.357	246	1
QSO B0329-385	2.437	2.008	2.380	75	1
HE 1158-1843	2.448	2.017	2.391	97	1
HE 1347-2457	2.599	2.149	2.539	313	1
QSO B1442+2931	2.660	2.203	2.599	107	5
QSO B0453-423	2.669	2.211	2.608	194	1
PKS 0329-255	2.696	2.234	2.635	97	1
QSO J0103+1316	2.721	2.256	2.659	218	4
HE 0151-4326	2.763	2.293	2.701	182	1
QSO B0002-422	2.769	2.298	2.707	211	1
HE 2347-4342	2.880	2.395	2.816	164	1
QSO B1107+4847	2.970	2.474	2.904	94	5
QSO J0407-4410	3.021	2.519	2.954	235	4
HS 1946+7658	3.058	2.551	2.991	156	1
HE 0940-1050	3.093	2.582	3.025	333	1,2
QSO B0420-388	3.126	2.610	3.057	138	1
QSO B0636+6801	3.180	2.658	3.111	107	5
QSO B1425+6039	3.180	2.658	3.111	140	5
QSO B1209+0919	3.291	2.755	3.220	30	3
PKS 2126-158	3.292	2.756	3.221	198	1
QSO B1422+2309	3.623	3.046	3.546	90	1,5
SDSS J1249-0159	3.630	3.052	3.553	85	3
QSO B0055-269	3.660	3.078	3.583	142	1
SDSS J1621-0042	3.710	3.122	3.632	159	3,4
QSO J1320-0523	3.717	3.128	3.639	154	3
PKS 1937-101	3.787	3.189	3.708	138	1,4
QSO J1646+5514	4.100	3.463	4.016	119	5
QSO B1055+4611	4.15	3.507	4.065	47	5
QSO B2237-0608	4.56	3.866	4.468	42	5

1 D’Odorico et al. (2010); 2 D’Odorico et al. (2016); 3 Calura et al. (2012); 4 This work; 5 Boksenberg & Sargent (2015)

smaller than 50 km s^{-1} have been merged. The merging process has been carried out in the following way: for each list of Si iv components corresponding to a single quasar, the velocity separations among all the lines have been computed and sorted in ascending order. If the smallest separation is less than $dv_{\text{min}} = 50 \text{ km s}^{-1}$, the two corresponding absorption lines are merged into a new line with column density equal to the sum of the column densities, and redshift equal to the average of the redshifts, weighted by the column density of the components. The velocity separations are then computed again and the procedure is iterated until the smallest separation becomes larger than dv_{min} . For consistency, the same merging process was applied to the XQ-100 sample and to the $z \sim 6$ XSHOOTER sample described in Sec. 2.2 and 2.3, respectively.

2.2 The XQ-100 sample

XQ-100 is a collection of 100 XSHOOTER spectra of quasars with $z_{\text{em}} \simeq 3.5-4.5$ observed in the context of the ESO Large Programme “Quasars and their absorption lines: a legacy survey of the high-redshift Universe with VLT/X-shooter” (P.I. Sebastian López). The list of objects is reported in Table 2. The sample spans the Si iv redshift interval $2.94 \leq z \leq 4.70$.

Spectra were obtained with a binning $\times 2$ along the dispersion direction and a slit of 0.9 arcsec in the VIS arm (where all the Si iv lines fall) corresponding to a nominal resolving power of $R \sim 8900$. Data reduction was carried out with a custom pipeline, while the manually placed continuum was determined by selecting points along the quasar continuum free of absorption (by eye) as knots for a cubic spline. Ninety percent of the spectra has $\text{SNR} \geq 20$ per pixel of 11 km s^{-1} at 1700 \AA rest frame. All the details can be found in López et al. (2016).

Our Si iv line sample was built based on Perrotta et al. (2016) and Berg et al. (2021). We revised those detections and fitted them with Voigt profiles, using the *fitlyman* context of the ESO MIDAS package (Fontana & Ballester 1995). During the line fitting process, we realized that many spectra had a resolving power significantly larger than the nominal one. As a consequence, we recomputed the value of R for each spectrum based on the average value of the seeing during the observations (reported in the ESO archive as *DIMM*) and assuming a linear relation between resolving power and slit width (equivalent in this case to the seeing average value). If $\langle \text{DIMM} \rangle < 0.9$ arcsec, the new resolving power is obtained as $R_{\text{new}} \sim (0.9/\langle \text{DIMM} \rangle) \times 8800$. The new resolving powers adopted in the fit are reported in Table 2. The resolution element varies between ~ 20 and 34 km s^{-1} .

For consistency with the high-resolution sample, we excluded from the XQ-100 Si iv collection those systems which are associated with the known DLAs studied in Berg et al. (2016). Our fiducial sample covers an absorption path of $\Delta X \simeq 221.8$ for a total of 385 detected Si iv absorption lines with $\log N(\text{Si iv}) \geq 12.5$. In the following, this sample will be called “XQ-100-noDLA”. We verified that the results are not significantly affected by the inclusion or exclusion of the Si iv lines associated with the DLAs.

2.3 The $z \sim 6$ XSHOOTER sample

This is a collection of ten XSHOOTER quasar spectra of which: 6 were already analysed in D’Odorico et al. (2013). ULAS J0148+0600 was analysed in Codoreanu et al. (2018) but we re-analysed the XSHOOTER spectrum in the ESO archive, and the last 3 spectra are published in this paper for the first time. The sample is reported in Table 3 and the log of observation for the new objects is in Table 4. In this sample, the Si iv is observable in the redshift range $4.96 \leq z \leq 6.40$. As for the XQ-100 sample, we have revised the resolution of the spectra based on the atmospheric conditions in which they were observed. The new resolving powers are reported in Table 3.

The three new quasars were reduced with the custom pipeline used for the XQ-100 spectra and analysed with the

Table 2. The XQ-100 quasar sample. The columns are the same as in Table 1 with the exception of the reference column, since all the spectra were presented in López et al. (2016) and the column R_{new} which reports the adopted resolving power if different from the nominal one.

Object	z_{em}	z_{min}	z_{max}	R_{new}	Object	z_{em}	z_{min}	z_{max}	R_{new}
J1332+0052	3.5082	2.9453	3.4336	—	J0211+1107	3.9734	3.3524	3.8911	10700
J1018+0548	3.5154	2.9516	3.4407	10400	J0214-0518	3.9770	3.3556	3.8947	9400
J1201+1206	3.5218	2.9572	3.4470	13400	J1032+0927	3.9854	3.3629	3.9029	10300
J1024+1819	3.5243	2.9594	3.4495	9800	J1542+0955	3.9863	3.3637	3.9038	10400
J1442+0920	3.5319	2.9660	3.4569	9900	J2215-1611	3.9946	3.3710	3.9120	15000
J0100-2708	3.5459	2.9783	3.4707	9900	J0255+0048	4.0033	3.3786	3.9205	10400
J1517+0511	3.5549	2.9862	3.4796	—	J0835+0650	4.0069	3.3817	3.9241	11600
J1445+0958	3.5623	2.9926	3.4868	10300	J0311-1722	4.0338	3.4053	3.9505	9700
J1202-0054	3.5924	3.0190	3.5164	—	J1323+1405	4.0537	3.4227	3.9701	10100
J1416+1811	3.5928	3.0193	3.5168	—	J0244-0134	4.0546	3.4235	3.9710	12000
J1524+2123	3.6002	3.0258	3.5241	—	J0415-4357	4.0732	3.4397	3.9893	9900
J1103+1004	3.6070	3.0318	3.5308	—	J0048-2442	4.0827	3.4481	3.9986	11400
J1117+1311	3.6218	3.0447	3.5453	—	J0959+1312	4.0916	3.4558	4.0074	—
J1037+2135	3.6260	3.0484	3.5495	—	J0121+0347	4.1252	3.4852	4.0404	—
J1249-0159 ^a	3.6289	3.0509	3.5523	—	J0003-2603	4.1254	3.4854	4.0406	—
J1042+1957	3.6302	3.0521	3.5536	—	J1037+0704	4.1271	3.4869	4.0423	—
J1126-0126	3.6346	3.0559	3.5579	—	J1057+1910	4.1284	3.4881	4.0436	11800
J0056-2808	3.6347	3.0560	3.5580	—	J0747+2739	4.1334	3.4924	4.0485	—
J1020+0922	3.6401	3.0607	3.5633	9900	J1110+0244	4.1456	3.5031	4.0605	9700
J0920+0725	3.6465	3.0663	3.5696	10100	J0132+1341	4.1523	3.5090	4.0671	9700
J1304+0239	3.6481	3.0677	3.5712	—	J2251-1227	4.1575	3.5135	4.0722	15000
J0818+0958	3.6564	3.0750	3.5794	11400	J0529-3552	4.1717	3.5259	4.0862	10700
J0057-2643 ^a	3.6608	3.0788	3.5837	9700	J0030-5129	4.1729	3.5270	4.0873	—
J0755+1345	3.6629	3.0807	3.5858	—	J0133+0400	4.1849	3.5375	4.0991	12000
J1053+0103	3.6634	3.0811	3.5863	—	J0153-0011	4.1948	3.5462	4.1089	—
J1108+1209	3.6789	3.0947	3.6015	9500	J2349-3712	4.2192	3.5675	4.1329	9700
J1421-0643	3.6885	3.1031	3.6109	—	J0403-1703	4.2267	3.5741	4.1402	12900
J1503+0419	3.6919	3.1061	3.6143	—	J0839+0318	4.2298	3.5768	4.1433	9500
J0937+0828	3.7035	3.1162	3.6257	10200	J0247-0556	4.2335	3.5800	4.1469	—
J1352+1303	3.7065	3.1188	3.6286	—	J0117+1552	4.2428	3.5882	4.1561	—
J1621-0042 ^a	3.7112	3.1229	3.6333	—	J2344+0342	4.2484	3.5931	4.1616	10500
J0833+0959	3.7162	3.1273	3.6382	9300	J1034+1102	4.2691	3.6112	4.1819	9100
J1320-0523 ^a	3.7172	3.1282	3.6392	9100	J0034+1639	4.2924	3.6316	4.2049	—
J1248+1304	3.7210	3.1315	3.6429	—	J0234-1806	4.3046	3.6423	4.2169	—
J1552+1005	3.7216	3.1320	3.6435	10400	J0113-2803	4.3145	3.6509	4.2266	11500
J1312+0841	3.7311	3.1404	3.6528	10400	J0426-2202	4.3289	3.6635	4.2408	—
J0935+0022	3.7473	3.1545	3.6688	—	J1058+1245	4.3413	3.6744	4.2529	—
J1658-0739	3.7496	3.1565	3.6710	—	J1633+1411	4.3650	3.6951	4.2763	10400
J1126-0124	3.7650	3.1700	3.6862	—	J0525-3343	4.3851	3.7127	4.2960	12800
J1336+0243	3.8009	3.2014	3.7215	11400	J1401+0244	4.4078	3.7326	4.3183	12200
J1013+0650	3.8086	3.2082	3.7291	14400	J0529-3526	4.4183	3.7418	4.3287	9500
J1135+0842	3.8342	3.2306	3.7542	—	J0955-0130	4.4185	3.7419	4.3289	10150
J0124+0044	3.8368	3.2329	3.7568	—	J0248+1802	4.4390	3.7599	4.3490	12000
J1331+1015	3.8522	3.2463	3.7719	11400	J0006-6208	4.4400	3.7607	4.3500	—
J0042-1020	3.8629	3.2557	3.7825	11600	J0714-6455	4.4645	3.7822	4.3741	15000
J1111-0804	3.9225	3.3079	3.8411	13400	J2216-6714	4.4793	3.7951	4.3887	9700
J0800+1920	3.9481	3.3303	3.8663	—	J1723+2243	4.5310	3.8404	4.4395	—
J1330-2522	3.9485	3.3306	3.8666	11300	J1036-0343	4.5311	3.8405	4.4396	10300
J0137-4224	3.9709	3.3502	3.8887	—	J2239-0552	4.5566	3.8628	4.4647	—
J1054+0215	3.9709	3.3502	3.8887	11300	J0307-4945	4.78	4.0583	4.6844	10300

python-based software *astrocook*³ (Cupani et al. 2020). We carried out line detection, continuum determination and then line identification and Voigt profile fitting in the context of *astrocook*. For consistency, we used *astrocook* also to repeat the fit of the absorption lines in the other quasars of the sample. The line parameters obtained with *astrocook* are consis-

tent within the measurement errors with those reported in D’Odorico et al. (2013) that were obtained within the *fitlyman* context of the ESO MIDAS package (Fontana & Ballester 1995). The 10 spectra allow to probe Si IV absorption lines with $\log N(\text{Si IV}) \geq 12.5$ along an absorption path $\Delta X \simeq 32.7$, in which a total of 22 lines have been detected.

In the following, we give a brief description of the new quasars and of the detected Si IV absorption systems, whose parameters are given in Table A1. The complete analysis of

³ <http://github.com/DAS-OATs/astrocook>

Table 3. The XSHOOTER $z \sim 6$ sample. The columns are the same as in Table 1.

Object	z_{em}	z_{min}	z_{max}	R_{new}	Ref.
SDSS J0836+0054	5.810	4.960	5.697	13100	1
ULAS J0148+0600	5.98	5.108	5.864	13300	2, 3
SDSS J1306+0356	6.0337	5.155	5.917	12000	1
SDSS J0818+1722	6.02	5.143	5.904	11000	1
CFHQS J1509-1749	6.1225	5.233	6.005	11800	1
ULAS J1319+0950	6.1330	5.242	6.015	13700	1
SDSS J1030+0524	6.308	5.395	6.187	12300	1
ATLAS J025-33	6.3379	5.422	6.216	11200	3
VDES J0224-4711	6.526	5.586	6.401	11200	3
PSO J036+03	6.5412	5.599	6.416	10700	3

1 D’Odorico et al. (2013); 2 Codoreanu et al. (2018); 3 This work

the absorption systems in the new spectra will be described in a forthcoming paper (Davies et al. in prep.).

ATLAS J025.6821-33.4627 (J0142-3327)

This object was discovered in the context of the VST ATLAS survey (Carnall et al. 2015). It has a redshift $z_{\text{em}} = 6.3379$ measured from the [C II] emission line (Decarli et al. 2018). It was observed with XSHOOTER at the VLT in October/November 2015 and in November 2018. We detect in the spectrum several C IV absorption systems of which two, at $z=5.64573$ and $z=5.76781$, have also an associated Si IV absorption.

VDES J0224-4711

This quasar, at $z = 6.526$, was discovered recently (Reed et al. 2017) and is the second most luminous quasar known at $z \geq 6.5$. It was observed with XSHOOTER at the VLT in November 2017, January 2018 and January/December 2019. Several C IV systems have been detected in this spectrum with that at $z=6.03082$ showing an associated Si IV absorption. We detect also a possible Si IV absorption at $z=5.55276$, the corresponding C IV transitions are not detected because they would fall in a very noisy region of the spectrum.

PSO J036.5078+03.0498 (J0226+0302)

Venemans et al. (2015) discovered this very bright quasar based on the imaging obtained by the Pan-STARRS1 Survey. The systemic redshift, $z = 6.5412$, was determined from the [C II] emission line (Decarli et al. 2018). Observations with XSHOOTER at the VLT were carried out in December 2017, January/November 2018 and January 2019. In this spectrum, two systems have both C IV and Si IV lines at $z=5.89869$ and $z=5.902399$.

2.4 Comparison between XSHOOTER and UVES spectra

In general, Si IV absorptions are relatively weak, so even if the resolution of XSHOOTER does not allow to resolve most of the metal lines, our measured column densities should not be significantly affected by unresolved saturation. To prove this statement, we have considered the Si IV absorption lines identified and fitted in the 4 quasars that are in common between

Table 4. Log of observations for the 3 new quasars at $z > 6.3$ observed with XSHOOTER. Columns 2 and 4 report the cumulative exposure time per target, per run. While columns 3 and 5 report the adopted slit width. They correspond to nominal resolving powers of $R \simeq 8900$ for 0.9" in the VIS, and $R \simeq 5600$ (8100) for 0.9" (0.6") in the NIR.

Program	Exp.T _{VIS} (sec)	slit _{VIS} (")	Exp.T _{NIR} (sec)	slit _{NIR} (")
<i>ATLAS J025.6821-33.4627</i>				
P096.A-0418 ^a	5580	0.9	5760	0.9JH
P0102.A-0154 ^b	14160	0.9	14400	0.6
<i>VDES J0224-4711</i>				
P0100.A-0625 ^b	4640	0.9	4800	0.9
P0102.A-0154 ^b	4720	0.9	4800	0.6
P1103.A-0817 ^b	24000	0.9	24000	0.6
<i>PSO J036.5078+03.0498</i>				
P0100.A-0625 ^b	4640	0.9	4800	0.9
P0102.A-0154 ^b	18880	0.9	19200	0.6

^a P.I. Shanks; ^b P.I. D’Odorico V.

Table 5. Results of the Si IV lines identification and fitting for the XSHOOTER spectra of J0148 and the 3 new quasars at $z > 6.3$.

z_{abs}	b (km s ⁻¹)	$\log N(\text{Si IV})$
<i>ULAS J0148+0600</i>		
5.12517 ± 0.00002	27 ± 2	12.77 ± 0.02
5.48778 ± 0.00003	24 ± 2	12.77 ± 0.03
<i>ATLAS J025.6821-33.4627</i>		
5.64574 ± 0.00004^a	5.0	12.23 ± 0.10
5.76786 ± 0.00004	12 ± 4	12.72 ± 0.04
<i>VDES J0224-4711</i>		
5.55276 ± 0.00004^a	26 ± 3	12.72 ± 0.03
6.03082 ± 0.00006	18 ± 5	12.95 ± 0.08
<i>PSO J036.5078+03.0498</i>		
5.89873 ± 0.00006	6.0	12.67 ± 0.09
5.90223 ± 0.00001	33 ± 8	12.86 ± 0.09

^a This line has not been considered in the analysis because its column density or redshift fall outside the considered ranges.

the high-resolution sample and the XQ-100 sample: J1249-0159, Q0055-269 (or J0057-2643), J1621-0042 and J1320-0523. In order to compare the measured column densities, due to the different resolutions of the two samples, we have computed the total column density of each absorption “system” obtained after the merging process described in Sec. 2.1. Results are reported in Fig. 2. All systems with column density $\log N(\text{Si IV}) \gtrsim 12.5$ have UVES and XSHOOTER measurements which are consistent within observational errors. As we will see in the following sections, our analysis will be based only on systems with $\log N(\text{Si IV}) \geq 12.5$ for which we are substantially complete given the minimum SNR of the analysed spectra; as a consequence we will assume that XSHOOTER column densities are reliable even though lines are probably not resolved in XSHOOTER spectra.

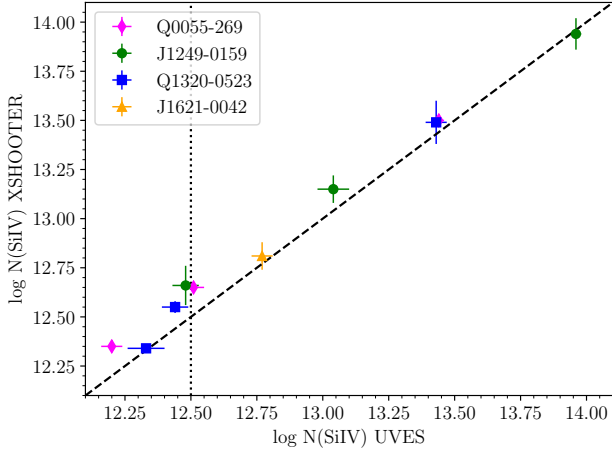


Figure 2. Comparison between the column densities obtained for the Si IV systems in the 4 quasars which are in common between the UVES/HIRES sample and the XQ-100 one. The vertical dotted lines marks the minimum Si IV column density we adopt for our computations and the dashed line indicate the 1:1 relation.

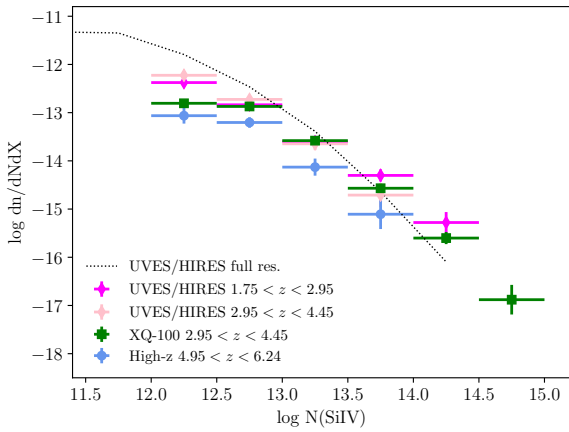


Figure 3. Column density distribution function for the Si IV absorptions in the UVES/HIRES (pink and magenta diamonds), XQ-100 (green squares) and $z \sim 6$ XSHOOTER (blue circles) samples. The dotted line indicates the CDDF of the original UVES/HIRES sample (before merging the lines closer than 50 km s^{-1}).

3 STATISTICS OF THE Si IV ABSORPTION LINES

3.1 Column density distribution function

The column density distribution function (CDDF), $f(N)$, is defined as the number of lines per unit column density and per unit redshift absorption path, dX (Tytler 1987). The redshift absorption path is used to remove the redshift de-

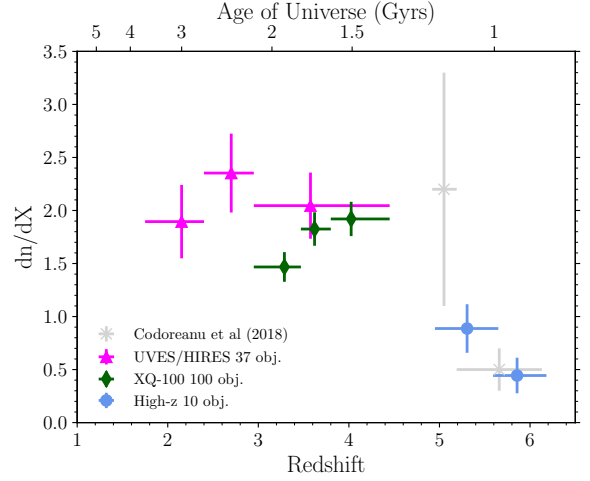


Figure 4. Number density for the Si IV absorptions detected in our three samples. Lines have been selected to have column densities $\log N(\text{Si IV}) \geq 12.5$ and redshifts in the range $1.75 \leq z \leq 6.24$. The light gray crosses are the results from Codoreanu et al. (2018).

pendence in the sample and put everything on a comoving coordinate scale. In the assumed cosmology it is defined as:

$$dX \equiv (1+z)^2 [\Omega_m (1+z)^3 + \Omega_\Lambda]^{-1/2} dz. \quad (1)$$

With the adopted definition, $f(N)$ does not evolve at any redshifts for a population whose physical size and comoving space density are constant.

The CDDF is a fundamental statistical property of absorption lines, similar for many aspects to the luminosity function for stars and galaxies.

The results of the computation of the CDDF for our three samples are shown in Fig. 3. In the figure, the CDDF of the original UVES/HIRES sample (before merging the lines closer than 50 km s^{-1}) is shown as a dotted line. The "full resolution" sample shows an increasing CDDF, suggesting a good completeness down to the $\log N(\text{Si IV}) = [11.5 - 12.0]$ column density bin, and then it flattens out. These values are in agreement with the column density thresholds derived from the SNR of the spectra in Section 2.1.

We observe that the number density of lines for the two UVES/HIRES redshift bins and for XQ-100-noDLA are consistent in the column density range $12.5 \leq \log N(\text{Si IV}) \leq 14.5$; at $\log N(\text{Si IV}) \leq 12.5$ the different behaviour is driven by the fact that the XQ-100-noDLA sample is not complete (e.g. Ellison et al. 2000); at $\log N(\text{Si IV}) \geq 14.5$ only the XQ-100-noDLA sample shows detected lines, attesting that these high column density lines are rare and a large number of lines of sight are needed to detect a significant number of them.

Comparing the CDDF at $z < 4.8$ with that at $z \geq 4.8$ computed with the $z \sim 6$ XSHOOTER sample, we remark that at high z the CDDF is systematically lower than at lower z by $\sim 0.3 - 0.5$ dex for all the column density bins between 12.0 and 14.0. The very low value at $12.0 \leq \log N(\text{Si IV}) \leq 12.5$ can still be explained with the incompleteness of the sample, while the lack of lines at $\log N(\text{Si IV}) \geq 14.5$ is consistent with the rarity of these lines and the low number of the inspected lines of sight.

In more detail, from the XQ-100-noDLA CDDF, a number density of 0.05 ± 0.01 (0.009 ± 0.006 , based on 2 lines) in the column density bin $[14.0, 14.5]$ ($[14.5, 15.0]$) can be derived. Based on the surveyed absorption paths, these number densities imply a number of absorption lines consistent with zero in the column density bin $[14.5, 15.0]$ for both the $z \sim 6$ XSHOOTER sample ($n = 0.3 \pm 0.2$) and the two inspected redshift bins of the UVES/HIRES sample ($n = 0.3 \pm 0.2$ and 0.2 ± 0.1). In the lower column density bin $[14.0, 14.5]$, the number of expected lines is consistent with $\sim 0 - 2$ and only in the case of the UVES/HIRES lower redshift bin, $z = [1.75, 2.95]$, we actually detect one Si IV absorption line.

3.2 Number density

We have also computed the number density of Si IV absorption lines with column densities $\log N(\text{Si IV}) \geq 12.5$ for which all samples have a high completeness rate. For all samples we have considered the Si IV systems defined as described in Sec. 2.1.

The number density has been computed as the number of lines (N_{lin}) in the considered redshift bin divided by the redshift absorption path (ΔX) obtained integrating eq. 1 in the redshift intervals contributed by each line of sight to the specific redshift bin. The results are shown in Fig. 4 and in Table 6. The high-resolution UVES-HIRES sample shows in the redshift range $1.75 \leq z \leq 4.45$ a behaviour which is consistent with a flat evolution with a possible hint of slightly decreasing number density toward lower redshifts. The XQ-100 sample which is characterized by the largest number of lines of sight and, accordingly, of absorption lines, is in agreement with the previous sample within observational errors. The lower value in the $z = [2.95, 3.47]$ redshift bin could be marginally affected by the fact that it covers the first order of the XSHOOTER VIS spectrum, which in general has a slightly lower SNR with respect to the rest of the investigated spectrum.

Considering now the $z \sim 6$ sample, the measured number density values in the two analysed redshift bins are consistent between themselves within measured errors. On the other hand, dn/dX at $z = [4.95, 5.65]$ is a factor of ~ 2 lower than the XQ-100 dn/dX value at $z = [3.90, 4.70]$ significant at 4.5σ , confirming that dn/dX evolved dramatically at $z > 4$.

4 THE REDSHIFT EVOLUTION OF THE Si IV MASS DENSITY

Finally, the CDDF can be integrated in order to obtain the cosmological mass density of Si IV in QSO absorption systems as a fraction of the critical density today, or the contribution of Si IV to the closure density:

$$\Omega_{\text{SiIV}} = \frac{H_0 m_{\text{SiIV}}}{c \rho_{\text{crit}}} \int N f(N) dN, \quad (2)$$

where $H_0 = 100 h \text{ km s}^{-1} \text{ Mpc}^{-1}$ is the Hubble constant, m_{SiIV} is the mass of a Si IV ion, c is the speed of light, $\rho_{\text{crit}} = 1.88 \times 10^{-29} h^2 \text{ g cm}^{-3}$ and $f(N)$ is the CDDF. The above integral can be approximated by the sum:

$$\Omega_{\text{SiIV}} = \frac{H_0 m_{\text{SiIV}}}{c \rho_{\text{crit}}} \frac{\sum_i N_i(\text{SiIV})}{\Delta X}, \quad (3)$$

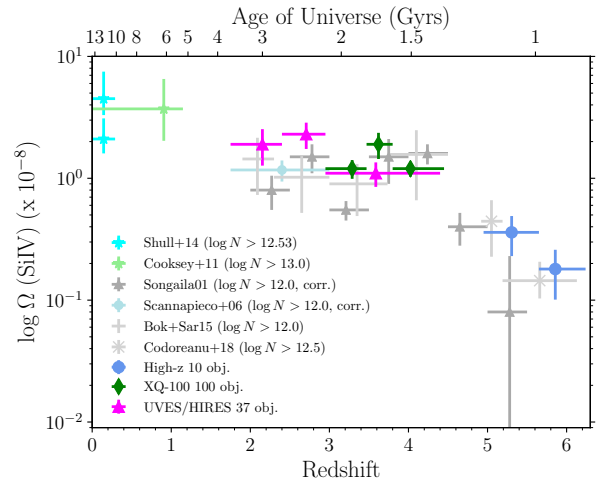


Figure 5. Cosmic mass density for the Si IV absorptions detected in our three samples. Lines have been selected to have column densities $\log N(\text{Si IV}) \geq 12.5$ and redshifts in the range $1.75 \leq z \leq 6.24$. Also shown are results by Shull et al. (2014) and Cooksey et al. (2011) for $z \leq 1$ and, for $z \geq 1.8$, the results by Songaila (2001), Scannapieco et al. (2006), Boksenberg & Sargent (2015) and Codoreanu et al. (2018). See the main text for further details.

Table 6. Si IV number density and cosmic mass density results considering $\log N(\text{Si IV}) \geq 12.5$.

z range	ΔX	N_{lin}	dn/dX	$\Omega(\text{Si IV})$ ($\times 10^{-8}$)
UVES/HIRES				
1.75 – 2.40	15.83	30	1.9 ± 0.3	1.9 ± 0.6
2.40 – 2.95	17.00	40	2.3 ± 0.4	2.3 ± 0.6
2.95 – 4.40	21.02	43	2.0 ± 0.3	1.1 ± 0.2
XQ-100 noDLA				
2.95 – 3.47	74.96	110	1.5 ± 0.1	1.2 ± 0.2
3.47 – 3.80	73.42	134	1.8 ± 0.2	1.9 ± 0.5
3.80 – 4.45	73.43	141	1.9 ± 0.2	1.2 ± 0.2
XSHOOTER $z \sim 6$				
4.95 – 5.65	16.91	15	0.9 ± 0.2	0.4 ± 0.1
5.65 – 6.24	15.77	7	0.4 ± 0.2	0.18 ± 0.08

with an associated fractional variance:

$$\left(\frac{\delta \Omega_{\text{SiIV}}}{\Omega_{\text{SiIV}}} \right)^2 = \frac{\sum_i [N_i(\text{SiIV})]^2}{[\sum_i N_i(\text{SiIV})]^2} \quad (4)$$

as proposed by Storrie-Lombardi et al. (1996). Note that the errors determined with this formula could be underestimated, in particular in the case of small line samples. In D’Odorico et al. (2010), we found that errors on Ω_{CIV} computed with a bootstrap technique were, at maximum, a factor of ~ 1.5 larger than those estimated with equation (4). For a fair comparison with previous results, however, we report in Table 6 the errors computed with equation (4).

It is interesting to point out the complementarity of the information conveyed by the number density, dn/dX , which is

heavily weighted toward abundant low-column density systems, and by the cosmological mass density, $\Omega_{\text{Si IV}}$, whose value depends mainly on the rare high-column density absorption lines.

As already observed for the CDDF and the number density of lines, Fig. 5 shows that the mass density parameter of Si IV increases by a factor $\sim 4 - 6$ moving from the redshift bin $z = [4.95, 5.65]$ to $z = [3.90, 4.70]$. In the redshift interval $2.94 \leq z \leq 4.70$ the evolution of $\Omega_{\text{Si IV}}$ is consistent with a flat behaviour, with a possible further increase toward $z \sim 1$ and the local Universe.

The low- z measurements were carried out by: Cooksey et al. (2011) using HST/STIS, HST/GHRS and FUSE data with Si IV lines in the redshift range $z \sim 0.0 - 1.15$ and $\log N(\text{Si IV}) \geq 13$, and by Shull et al. (2014) using HST/COS spectra for Si IV lines in the redshift range $z \sim 0.0 - 0.29$ with $\log N(\text{Si IV}) \geq 12.53$. The reported values correspond to two Si IV samples obtained with HST/STIS ($\Omega_{\text{Si IV}} = 4.5_{-1.2}^{+3.0} \times 10^{-8}$) and with HST/COS ($\Omega_{\text{Si IV}} = 2.1_{-0.5}^{+1.0} \times 10^{-8}$).

5 OUR RESULTS INTO CONTEXT

5.1 Comparison with previous Si IV results

The statistical quantity which is more safely comparable between different samples of absorption lines is the cosmic mass density, since it depends less on the resolution and the adopted fitting technique.

In Fig. 5, we report our measurements and previous determinations of $\Omega_{\text{Si IV}}$ at lower and comparable redshifts. Our results are in good agreement with the Songaila (2001) data, corrected for the different cosmology (see also Songaila 2005, based on the pixel optical depth technique).

Scannapieco et al. (2006) analysed a sample of 19 UVES spectra which are included in our high-resolution sample and give in their paper a value of $\Omega_{\text{Si IV}} = (0.6 \pm 0.12) \times 10^{-8}$ at $\langle z \rangle = 2.4$, which is alarmingly lower than our result. A careful revision of their paper revealed a mistake in the computation of the normalization factor of $\Omega_{\text{Si IV}}$ whose correction determines the new value $1.17 \pm 0.23 \times 10^{-8}$, consistent with our points.

The cosmic mass density for Si IV computed by Boksenberg & Sargent (2015) is based on a sample of 9 high-resolution Keck/HIRES quasar spectra. We have included the quasars lines of sight of BS15 in our sample, with the aim of extending the high-redshift coverage. This is reflected in Fig. 5 by the optimal consistency between our points and those of BS15.

Codoreanu et al. (2018) computed the statistical properties of Si IV absorption lines approaching $z \sim 6$. They considered a sample of 4 quasars all observed with XSHOOTER: ULAS J0148+0600, SDSS J1306+0356, ULAS J1319+0950 which are also part of our sample, and SDSS J0927+2001 ($z_{\text{em}} = 5.79$). They found 7 Si IV systems with column density $\log N(\text{Si IV}) \geq 12.5$ in the redshift range $4.92 \leq z \leq 6.13$, of which 5 have $z \geq 5.19$. As we can see from Fig. 4 and 5 our results are consistent with their findings within the observational errors.

Table 7. C IV number density and cosmic mass density results for the high resolution sample (D’Odorico et al. 2010) and for the XSHOOTER $z \sim 6$ sample (D’Odorico et al. 2013) considering column densities $\log N(\text{C IV}) \geq 13.0$ and adopting the same redshift bins used for Si IV with the exception of the bin $z = [4.50, 4.95]$ which is only covered for C IV absorptions.

z range	ΔX	N_{lin}	dn/dX	$\Omega(\text{C IV})$ ($\times 10^{-8}$)
UVES/HIRES				
1.75 – 2.40	32.43	127	3.9 ± 0.3	14 ± 3
2.40 – 2.95	21.32	90	4.2 ± 0.4	14 ± 3
2.95 – 4.45	23.98	102	4.2 ± 0.4	6.1 ± 0.8
XSHOOTER $z \sim 6$				
4.50 – 4.95	12.21	53	4.3 ± 0.6	2.9 ± 0.5
4.95 – 5.65	23.73	41	1.7 ± 0.3	2.0 ± 0.8
5.65 – 6.24	16.28	14	0.9 ± 0.2	0.7 ± 0.3

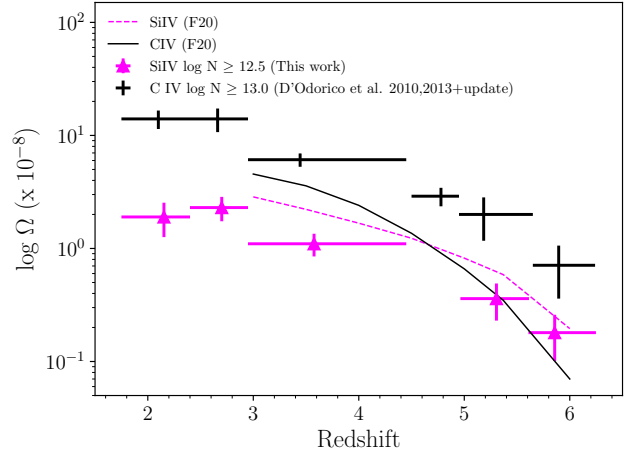


Figure 6. Comparison of the cosmic mass density parameters, Ω , for Si IV and C IV (D’Odorico et al. 2010, 2013, this work) among themselves and with the predictions of the simulations by Finlator et al. (2020).

5.2 Comparison with C IV and O I statistics

The statistical properties of C IV lines were the first to be studied thanks to the large available samples. In D’Odorico et al. (2013), we investigated the evolution with redshift of the C IV column density distribution function and cosmic mass density parameter up to $z \sim 6$. Both quantities increase significantly between $z \sim 6$ and 5 and then stay approximately constant in the range $2.0 \lesssim z \lesssim 5.0$. More recent studies (Codoreanu et al. 2018; Meyer et al. 2019) confirm these results.

The cosmic mass densities of Si IV absorbers with $\log N \geq 12.5$ estimated in this work and of C IV systems with $\log N(\text{C IV}) \geq 13.0$ are compared in Fig. 6. The choice of the C IV column density threshold depends on the Si IV column density threshold and on the observation that, in particular at $z \gtrsim 5$, the average ratio of Si IV/C IV column densities in log is

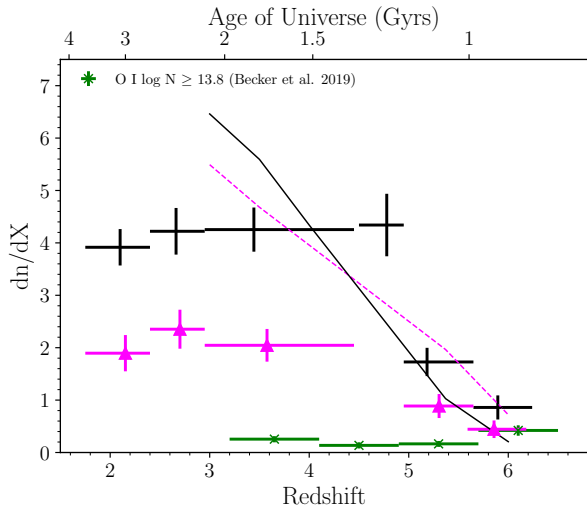


Figure 7. Number densities, dn/dX , of O I (green crosses, [Becker et al. 2019](#)), Si IV and C IV ([D’Odorico et al. 2010, 2013](#), this work) as a function of redshift, compared with the predictions for Si IV and C IV by [Finlator et al. \(2020\)](#). Symbols and lines are the same of Fig. 6.

~ -0.5 ([D’Odorico et al. 2013](#)). Ω_{CIV} has been computed in the same redshift bins adopted for Ω_{SiIV} and it is based on the UVES/HIRES sample from [D’Odorico et al. \(2010\)](#) and on the $z \sim 6$ XSHOOTER sample from [D’Odorico et al. \(2013\)](#). The $z \sim 6$ XSHOOTER sample has been updated with the addition of the C IV lines of ULAS J0148+0600 ([Codoreanu et al. 2018](#)) and of those of the three new quasars analysed in this work⁴. The two cosmic mass densities evolve with redshift in a very similar way, with an approximately constant ratio in the whole redshift range.

In Fig. 7, we compare dn/dX for Si IV absorbers with $\log N \geq 12.5$, estimated in this work, with the number densities of O I systems with $\log N(\text{O I}) \geq 13.8$ ([Becker et al. 2019](#)) and C IV absorbers with $\log N(\text{C IV}) \geq 13.0$. Si IV traces the C IV behaviour quite closely at all redshifts, with on average a factor ~ 2 less lines in each redshift bin. The increase of dn/dX with decreasing redshift for C IV is generally ascribed to the combination of the increase of the ionization status and the increase of the average metallicity of the gas, as we approach the peak of star formation (e.g. [Finlator et al. 2015](#); [Maiolino & Mannucci 2019](#)). On the other hand, O I shows a decrease at $z < 5.7$, then a constant behaviour to redshift 4 and a possible increase for $z < 4$. The decrease of O I number density at $z < 5.7$ can only be explained by a variation in the physical properties of the gas that is transitioning from a relatively neutral state to higher ionization states ([Doughty & Finlator 2019](#)).

The fact that Si IV and O I number densities coincide in the highest redshift bin does not imply that they trace the same absorbers, this is seen when inspecting absorption systems in our sample and also in other works (e.g. [Becker et al. 2019](#)). A detailed analysis of the column density ratios of different

⁴ The corresponding lists of C IV absorbers are reported in the Appendix.

Table 8. Our comparison simulations. The different columns report: the simulation reference (see text); the box size; the number of gas resolution elements when the simulation starts; the model for the ultraviolet ionizing background; the mass-loading factor; the wind velocity for a $M_b = 10^9 M_\odot$ galaxy at $z = 5$ and the cosmological power spectrum normalization.

ref	box (Mpc/h)	N_{gas}	UVB (km/s)	η_{10}	v_{wind} (Mpc/h)	σ_8
O09	16	512^3	HM01	3.96	82.3	0.83
G17	18	512^3	HM12	11.3	110.9	0.816
R16	100	1504^3	HM01	–	–	0.8288
F20	15	640^3	–	6.47	104	0.8159

ions in the same absorption systems will be carried out in a further work. It is interesting to see the sudden increase of the C IV number density in the redshift bin $z = [4.5, 4.95]$, which unfortunately cannot be covered by the present Si IV sample.

5.3 Comparison with simulation predictions

We now compare our results on the evolving Si IV and C IV abundances against the predictions from the four cosmological hydrodynamic simulations in the literature which computed the Si IV observables we have measured. For reference, we have summarized the simulations’ relevant physical and numerical parameters in Table 8.

Large box sizes account more completely for the rare, high-column density systems that dominate Ω_{SiIV} and Ω_{CIV} , while high mass resolution accounts more completely for the weak systems that dominate dn/dX ([Keating et al. 2016](#); [Finlator et al. 2020](#)). Note that an increase of the mass-loading factor⁵ suppresses the star formation efficiency and the CGM metallicity, decreasing the abundance of high-ionization metal absorbers ([Rahmati et al. 2016](#), R16). On the other hand, the wind speed regulates the ability of galactic outflows to heat the CGM as well as the fraction of ejecta that travels to the virial radius. The predicted CGM metallicity is proportional to the metal yield, which is uncertain by roughly a factor of two ([Wiersma et al. 2009](#)).

[Oppenheimer, Davé & Finlator \(2009, O09\)](#) extract absorber catalogs using a homogeneous UVB ([Haardt & Madau 2001](#), HM01) and a “bubble” model in which the UVB is determined by the nearest galaxy. Comparing with their Figure 11, both models overpredict Ω_{SiIV} at $z \sim 5$ and 6 by $2-3\sigma$. By contrast, they are in good agreement with Ω_{CIV} at the same redshifts. These results could indicate that the assumed silicon yield is too high. Alternatively, they could indicate that the overall CGM metallicity is too high owing to O09’s low mass-loading factor. In this case, the agreement with Ω_{CIV} would indicate that the adopted HM01 UVB is weak at the high energies that regulate C IV, cancelling the effect of the high metallicity.

The reference simulation of R16 incorporates a lower mass resolution and a larger cosmological volume than the other

⁵ The mass-loading factor, η_{10} , quantifies the ratio of the rate at which a galaxy ejects its interstellar medium (ISM) to its star formation rate.

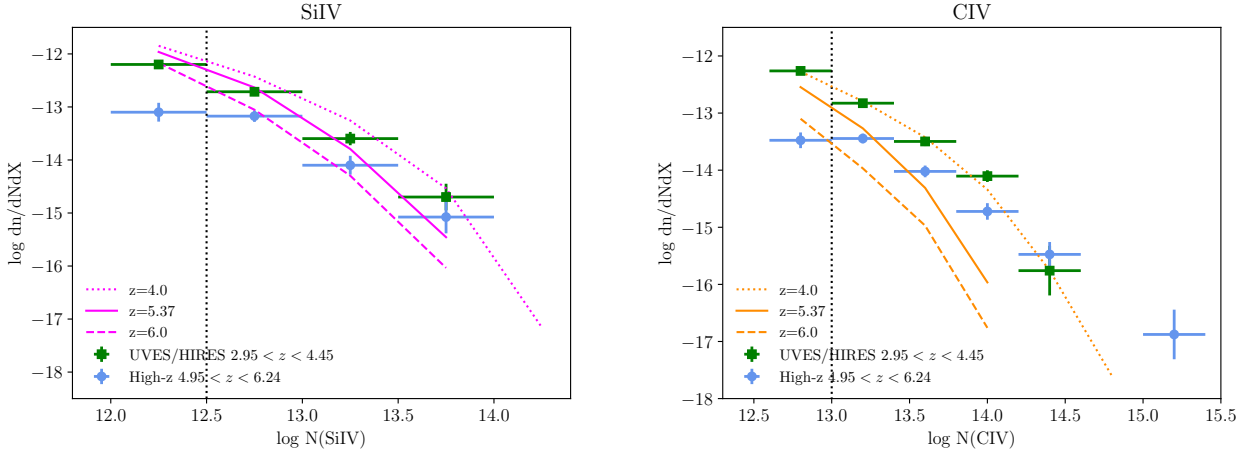


Figure 8. Predictions by Finlator et al. (2020) for the CDDF of absorbers at three different redshifts, $z = 4.0, 5.37$ and 6 , compared with: (Left panel) the CDDF of the Si IV absorbers in the UVES/HIRES sample (green squares) and in the high- z sample (light blue circles) and (Right panel) the CDDF of the C IV absorbers in the high-resolution sample from D’Odorico et al. (2010, green squares) and in the high- z sample (D’Odorico et al. 2013, this work, light blue circles).

three models, making it less complete for weak systems and more complete for strong ones. Its feedback model enables galactic outflows to form self-consistently, hence the mass-loading factor and wind velocities are not parameterized (Dalla Vecchia & Schaye 2012). The predicted redshift evolution of both the Si IV column density distribution function and Ω_{SiIV} are in qualitative agreement with our observations. By contrast, both quantities are underpredicted for C IV, particularly at $z > 3.5$. Our results confirm that this C IV underprediction, previously noted by R16, does not reflect observational sample size limitations. In analogy with our conclusions from O09, we find that either the assumed carbon yield is too low (at $z > 3.5$), or the predicted overall CGM metallicity is realistic while the HM01 UVB is, as in the case of O09, too weak at high energies.

In the fiducial model of Garcia et al. (2017, G17), the high mass-loading factor suppresses star formation and hence the CGM metallicity. On the other hand, the high wind speeds heat the CGM efficiently. We therefore expect a partial cancellation between the impacts of low metallicity and high temperature on high-ionization CGM absorbers. Codoreanu et al. (2018) find that the Si IV CDDF predicted by this model agrees with their observations in the redshift bin $z = [4.92, 6.13]$ up to column densities of $\log N(\text{Si IV}) = 13.5$, while possibly overproducing stronger systems. The higher column densities probed by our study enable us to confirm that the G17 Si IV CDDF is too flat, overpredicting observations at column densities exceeding $\log N(\text{Si IV}) \sim 14$. Ω_{SiIV} is consequently overpredicted by roughly an order of magnitude when integrating over columns up to $\log N(\text{Si IV}) = 15$. The predicted redshift evolution of Ω_{SiIV} may also be more gradual than observed: G17 predict that it drops by $\approx 2\times$ from $z = 4 \rightarrow 6$ (Figure 8 of Codoreanu et al. 2018), whereas our observations indicate a factor $\sim 2.5 - 5$ decline over the same interval. Much of this decline occurs at $z > 5$, where observations remain the most challenging.

Finally, the simulation by Finlator et al. (2020, F20) combines a feedback model in which the adopted wind

speeds and mass-loading factor are intermediate between G17 and O09 with a treatment for a self-consistent, spatially-inhomogeneous UVB that yields a realistic reionization history and post-reionization UVB amplitude.

Comparisons with D’Odorico et al. (2013) showed that, under the assumption of ionization-bounded escape (see F20 and Zackrisson, Inoue, & Jensen 2013), the predictions by F20 underproduce strong C IV absorbers while roughly reproducing strong Si IV absorbers. The improved Si IV sample presented in this work confirms the result of F20. The missing C IV and Si IV gas is found in lower ionization states. Indeed, F20 show that increasing ionization (density-bounded model) improves the agreement with the observed C IV and Si IV CDDF but worsen the agreement with the C II absorber statistics (their Fig. 7).

Fig. 6 shows that, at all redshifts, the F20 simulation accounts for the overall Si IV mass density. The predicted Ω_{SiIV} normalization is slightly high, but this offset falls within the range of uncertainty associated with the unknown metal yields. By contrast, the predicted Ω_{CIV} evolution is steeper than observed, suggesting that the model cannot account for the observed early assembly of strong C IV systems.

Fig. 8 reveals that the predicted Si IV CDDF is somewhat too steep, overproducing faint absorbers to a degree that increases with time (also seen in Fig. 7). Further work will be required to determine what portion of this discrepancy reflects observational incompleteness, which manifests as a clear flattening in the observed Si IV CDDF for $\log N(\text{Si IV}) < 12.5$. The C IV CDDF is likewise too steep. At $z > 4$, this problem is compensated by its low normalization, leading to tolerable agreement with the observed dn/dX (see Fig. 7). At $z < 4$, the overabundance of weak C IV systems causes the model to overproduce dn/dX , in agreement with results from a complementary study that focused on the observed C IV equivalent width distribution (Hasan et al. 2020).

6 SUMMARY

In this paper, we have computed the statistical properties of a sample comprising almost 600 Si IV absorption lines with column densities $\log N(\text{Si IV}) \geq 12.5$, detected in the spectra of 147 quasars at redshifts between $2.1 \lesssim z_{\text{em}} \lesssim 6.5$.

The main results of this work are the following:

- The column density distribution function of Si IV absorption lines does not show significant variations in the redshift range $1.7 \lesssim z \lesssim 4.7$, while for the highest redshift bin $4.95 \leq z \leq 6.24$ it is systematically lower at all column densities (Fig. 3). The same behaviour was observed for C IV absorption lines (e.g. D’Odorico et al. 2013).
- The number density of lines per unit redshift absorption path, dn/dX , shows a small increase with redshift between $z \sim 6$ and $z \sim 5.3$ and then a jump of a factor ~ 2.5 at $z < 4.7$. Then, the number density remains approximately constant to $z \sim 2$.
- The comparison of the number densities of Si IV, C IV, and O I shows that Si IV lines with $\log N(\text{Si IV}) \geq 12.5$ and C IV lines with $\log N(\text{C IV}) \geq 13.0$ have a very similar evolution with redshift, while O I shows a mild decrease for $z < 5.7$ as reported in Becker et al. (2019).
- The Si IV cosmic mass density shows a smooth increase from redshift ~ 6 to 3.5 (of a factor ~ 5) and then it stays constant to $z \sim 2$.
- The comparison of $\Omega_{\text{Si IV}}$ with $\Omega_{\text{C IV}}$ shows a similar evolution in redshift with an almost constant ratio.
- Finally, the examination of the predictions from cosmological, hydro-dynamical simulations indicates that the observed CDDF and cosmic mass density of Si IV are well reproduced when the same quantities for C IV are underpredicted. In those cases in which feedback (or other properties) are boosted to reproduce C IV, the Si IV mass density is generally overproduced. The C IV line incidence predicted by Finlator et al. (2020) is generally consistent with observations while the Si IV line incidence is roughly consistent with observations at $z = 6$ but then grows too rapidly down to at least $z = 3$. Meanwhile, the predicted C IV CDDF of the F20 model is too steep, particularly at early times, while the Si IV CDDF has roughly the correct shape.

The results presented in this work probe new observational ground to constrain future models and advance our understanding of the distribution of metals and the enrichment mechanism of CGM and IGM.

At $z \gtrsim 5$, we are still dealing with low number statistics and the results are relatively uncertain. This problem should soon be solved by the XQR-30 survey that will provide a sample of 30 new QSO spectra in the redshift range $z_{\text{em}} = 5.8 - 6.6$ obtained with XSHOOTER at the VLT in the context of an ESO Large Programme (1103.A-0817, P.I. V. D’Odorico) whose observations are almost complete.

In the longer run, when high-resolution spectrographs will be available at 30-40m class telescopes (e.g. Marconi et al. 2021) it will be possible to carry out more detailed studies on $z \sim 6$ metal absorption lines with the resolution and column density ranges reachable today with 8-10m class telescope at $z \sim 2 - 4$. Doughty et al. (2018) have shown that larger ranges in column densities for C IV and Si IV will allow to better distinguish between different UVB models at $z \sim 6$.

ACKNOWLEDGMENTS

We are thankful to the anonymous referee who has provided insightful comments to the paper allowing us to improve it sensibly. This work is based in part on observations collected at the European Southern Observatory Very Large Telescope, Cerro Paranal, Chile – Programmes Programs 65.O-0296, 166.A-0106, 069.A-0529, 079.A-0226, 084.A-0390, 084.A-0550, 085.A-0299, 086.A-0162, 087.A-0607, 268.A-5767, 189.A-0424, 096.A-0418, 0100.A-0625, 0102.A-0154, 0103.A-0817 and 1103.A-0817. Further observations were made at the W.M. Keck Observatory, which is operated as a scientific partnership between the California Institute of Technology and the University of California; it was made possible by the generous support of the W.M. Keck Foundation. The authors wish to recognize and acknowledge the very significant cultural role and reverence that the summit of Maunakea has always had within the indigenous Hawaiian community. S.L. acknowledges support by FONDECYT grant 1191232. KF acknowledges support from the National Science Foundation (NSF) via Award Number 2006550. The Technicolor Dawn simulations were enabled by the Extreme Science and Engineering Discovery Environment, which is supported by NSF grant number ACI-1548562. The Cosmic Dawn Center is funded by the Danish National Research Foundation.

DATA AVAILABILITY

All the ESO VLT raw spectra used in this paper are publicly available from the ESO archive. The reduced UVES spectra are available in the SQUAD data base (Murphy et al. 2019). The reduced XQ-100 spectra are available from the ESO archive, in the Phase 3 Data Releases section. The lists of fitted absorption lines underlying the obtained results, which are not published in this paper or available from the literature will be shared on reasonable request to the corresponding author.

REFERENCES

- Adelberger K. L., Shapley A. E., Steidel C. C., Pettini M., Erb D. K., Reddy N. A., 2005, *ApJ*, 629, 636
- Barai P., Viel M., Borgani S., Tescari E., Tornatore L., Dolag K., Killedear M., et al., 2013, *MNRAS*, 430, 3213
- Becker G. D. et al. 2019, *ApJ*, 883, 163
- Berg T. A. M., Fumagalli M., D’Odorico V., Ellison S. L., López S., Becker G. D., Christensen L., et al., 2021, *MNRAS*, 502, 4009
- Berg T. A. M., Ellison S. L., Sánchez-Ramírez R., Prochaska J. X., Lopez S., D’Odorico V., Becker G., et al., 2016, *MNRAS*, 463, 3021
- Bergeron J., et al., 2004, *ESO The Messenger*, 118, 40
- Bernstein R. M., Burles S. M., Prochaska J. X., 2015, *PASP*, 127, 911.
- Birnboim Y., Dekel A., 2003, *MNRAS*, 345, 349
- Boksenberg A., Sargent W. L. W., 2015, *ApJS*, 218, 7
- Bordoloi R., Tumlinson J., Werk J. K., Oppenheimer B. D., Peeples M. S., Prochaska J. X., Tripp T. M., Katz N., et al., 2014 *ApJ*, 796, 136
- Calura F., Tescari E., D’Odorico V., Viel M., Cristiani S., Kim T.-S., Bolton J. S., 2012, *MNRAS*, 422, 3019
- Calura F., Matteucci F., 2006, *MNRAS*, 369, 465
- Carnall A. C., et al. 2015, *MNRAS*, 451, L16

- Carswell R. F., Webb J. K., 2014, VPFIT, Astrophysics Source Code Library, record ascl:1408.015
- Cen R. & Chisari N. E., 2011, *ApJ*, 731, 11
- Codoreanu A., Ryan-Weber E. V., García L. A., Crighton N. H. M., Becker G. D., Pettini M., Madau P., Venemans B., 2018, *MNRAS*, 481, 4940
- Cooksey K. L., Kao M. M., Simcoe R. A., O’Meara J. M., Prochaska J. X., 2013, *ApJ*, 763, 37
- Cooksey K. L., Prochaska J. X., Thom C., Chen H.-W. 2011, *ApJ* 729, 87
- Cooksey K. L., Thom C., Prochaska J. X., Chen H.-W., 2010, *ApJ*, 708, 868
- Cooper T. J., Simcoe R. A., Cooksey K. L., Bordoloi R., Miller D. R., Furesz G., Turner M. L., Bañados E., 2019, *ApJ*, 882, 77
- Cowie L.L., Songaila A., Kim T.-S., Hu E.M., 1995, *AJ*, 109, 1522
- Cupani G., D’Odorico V., Cristiani S., Russo S. A., Calderone G., Taffoni G., 2020, *SPIE*, 11452, 114521U
- Dalla Vecchia C., Schaye J., 2012, *MNRAS*, 426, 140
- Decarli R., et al., 2018, *ApJ*, 854, 97
- Dekker H., D’Odorico S., Kaufer A., Delabre B., Kotzlowski H., 2000, *SPIE*, 4008, 534
- D’Odorico V. et al., 2016, *MNRAS*, 463, 2690
- D’Odorico V. et al., 2013, *MNRAS*, 435, 1198
- D’Odorico V., Calura F., Cristiani S., Viel M., 2010, *MNRAS*, 401, 2715
- Doughty C., Finlator K., Oppenheimer B. D., Davé R., Zackrisson E., 2018, *MNRAS*, 475, 4717
- Doughty, C. & Finlator, K., 2019, *MNRAS*, 489, 2755
- Ellison S. L., Songaila A., Schaye J., Pettini M., 2000, *AJ*, 120, 1175
- Faucher-Giguère C.-A., Kereš D., Ma C.-P., 2011, *MNRAS*, 417, 2982
- Finlator K., Doughty C., Cai Z., Díaz G., 2020, *MNRAS*, 493, 3223
- Finlator K., Keating L., Oppenheimer B. D., Davé R., Zackrisson E., 2018, *MNRAS*, 480, 2628
- Finlator K., Thompson R., Huang S., Davé R., Zackrisson E., Oppenheimer B. D., 2015, *MNRAS*, 447, 2526
- Fontana A., Ballester P., 1995, *ESO The Messenger*, 80, 37
- Fossati M., Fumagalli M., Lofthouse E. K., Dutta R., Cantalupo S., Arrighi Battaia F., Fynbo J. P. U., et al., 2021, *MNRAS*, 503, 3044
- Fossati M., et al. 2019, *MNRAS*, 490, 1451
- García L. A., Tescari E., Ryan-Weber E. V., Wyithe J.S.B., *MNRAS*, 470, 2494
- Haardt F., Madau P., 2012, *ApJ*, 746, 125
- Haardt F., Madau P., 2001 in “Clusters of galaxies and the high redshift Universe observed in X-rays: recent results of XMM-Newton and Chandra”, XXXVth Rencontres de Moriond, eds. D.M. Neumann & J.T.T. Van
- Hasan F., Churchill C. W., Stemock B., Mathes N. L., Nielsen N. M., Finlator K., Doughty C., et al., 2020, *ApJ*, 904, 44
- Keating L. C., Puchwein E., Haehnelt M. G., Bird S., Bolton J. S., 2016, *MNRAS*, 461, 606
- Kereš D., Katz N., Weinberg D. H., Davé R., 2005, *MNRAS*, 363, 2
- Johnson S. D., Chen H.-W., Mulchaey J. S., Schaye J., Straka L. A. 2017, *ApJL*, 850, L10
- Liang C. J., Chen, H.-W., 2014, *MNRAS*, 445, 2061
- Lofthouse E. K., Fumagalli M., Fossati M., O’Meara J. M., Murphy M. T., Christensen L., Prochaska J. X., et al., 2020, *MNRAS*, 491, 2057
- López S., Tejos N., Barrientos L. F., Ledoux C., Sharon K., Katsianis A., Florian M. K., et al., 2020, *MNRAS*, 491, 4442
- López S. et al., 2018, *Nature*, 554, 493
- López S. et al., 2016, *A&A*, 594, 91
- Madau P., Ferrara A., Rees M. J., 2001, *ApJ*, 555, 92. doi:10.1086/321474
- Maiolino R., Mannucci F., 2019, *A&ARv*, 27, 3
- Marconi A., Abreu M., Adibekyan V., Aliverti M., Allende Prieto C., Amado P., Amate M., et al., 2021, *Msngr*, 182, 27
- Meyer R.A., Bosman S. E. I., Kakiichi K., Ellis R. S., 2019, *MNRAS*, 483, 19,
- Mongardi C., Viel M., D’Odorico V., Kim T.-S., Barai P., Murante G., Monaco P., 2018, *MNRAS*, 478, 3266
- Muratov A. L., Kereš D., Faucher-Giguère C.-A., Hopkins P. F., Ma X., Anglés-Alcázar D., Chan T. K., et al., 2017, *MNRAS*, 468, 4170
- Murphy M. T., Kacprzak G. G., Savorgnan G. A. D., Carswell R. F., 2019, *MNRAS*, 482, 3458
- Nelson D., Vogelsberger M., Genel S., Sijacki D., Kereš D., Springel V., Hernquist L., 2013, *MNRAS*, 429, 3353
- Oppenheimer B.D., Davé R., Finlator K., 2009, *MNRAS*, 396, 729
- Oppenheimer B.D., Davé R., 2006, *MNRAS*, 373, 1265
- Péroux C., Howk J. C., 2020, *ARA&A*, 58, 363
- Perrotta S., D’Odorico V., Prochaska J. X., Cristiani S., Cupani G., Ellison S., López S., et al., 2016, *MNRAS*, 462, 3285
- Prochaska J. X., Weiner B., Chen H.-W., Mulchaey J., Cooksey K., 2011, *ApJ*, 740, 91
- Rahmati A., Schaye J., Crain R. A., Oppenheimer B. D., Schaller M., Theuns T., 2016, *MNRAS*, 459, 310
- Reed S. L. et al. 2017, *MNRAS*, 468, 4702
- Rudie G. C., Steidel C. C., et al. 2019, *ApJ*, 885, 61
- Ryan-Weber E.V., Pettini M., Madau P., Zych B.J., 2009, *MNRAS*, 395, 1476
- Sánchez-Ramírez R., et al. 2016 *MNRAS* 456, 4488
- Savage B. D., Sembach K. R., 1991, *ApJ*, 379, 245
- Scannapieco E., et al., 2006, *MNRAS*, 365, 615
- Schaye J., Aguirre A., Kim T.-S., Theuns T., Rauch M., Sargent W.L.W., 2003, *ApJ*, 596, 768
- Shull J. M., Danforth C. W., Tilton E. M. 2014, *ApJ*, 796, 49
- Simcoe R. A. et al., 2011, *ApJ*, 743, 21
- Songaila A., 2005, *AJ*, 130, 1996
- Songaila A., 2001, *ApJ*, 561, L153
- Steidel C. C., et al., 2010, *ApJ*, 717, 289
- Storrie-Lombardi L., McMahon R.G., Irwin M., 1996, *MNRAS*, 283, 79
- Suresh J., Bird S., Vogelsberger M., Genel S., Torrey P., Sijacki D., Springel V., et al., 2015, *MNRAS*, 448, 895
- Tescari E., Viel M., D’Odorico V., Cristiani S., Calura F., Borgani S., Tornatore L., 2011, *MNRAS*, 411, 826
- Theuns T., 2021, *MNRAS*, 500, 2741
- Tumlinson J., Thom C., Werk J. K., Prochaska J. X., Tripp T. M., Weinberg D. H., Peebles M. S., O’Meara J. M., et al., 2011, *Science*, 334, 948
- Turner M. L., Schaye J., Crain R. A., Theuns T., Wendt M., 2016, *MNRAS*, 462, 2440
- Turner M. L., Schaye J., Steidel C. C., Rudie G. C., Strom A. L., 2014, *MNRAS*, 445, 794
- Tytler D., Fan X.-M., Burles S., Cottrell L., Davis C., Kirkman D., Zuo L., 1995, in *QSO Absorption Lines*, ed. G.Meylan (Springer-Verlag), 289
- Tytler D., 1987, *ApJ*, 321, 49
- van de Voort F., Schaye J., Booth C. M., Haas M. R., Dalla Vecchia C., 2011, *MNRAS*, 414, 2458
- van de Voort, F., Schaye, J., Altay, G., et al. 2012, *MNRAS*, 421, 2809
- Venemans B. P. et al., 2015, *ApJ*, 801, L11
- Werk J. K., Prochaska J. X., Tumlinson J., et al. 2014, *ApJ*, 792, 8
- Wiersma R. P. C., Schaye J., Theuns T., Dalla Vecchia C., Tornatore L., 2009, *MNRAS*, 399, 574
- Zackrisson E., Inoue A. K., Jensen H., 2013, *ApJ*, 777, 39

Table A1. New C IV absorbers added to the high- z sample.

z_{abs}	b (km s $^{-1}$)	$\log N(\text{Si IV})$
<i>ATLAS J025.6821-33.4627</i>		
4.78570 ± 0.00006	45 ± 6	13.26 ± 0.03
4.86459 ± 0.00002	23 ± 1	13.15 ± 0.02
4.89616 ± 0.00007^a	–	13.39 ± 0.02
4.93643 ± 0.00002^a	–	13.17 ± 0.02
5.18942 ± 0.00004^a	–	13.43 ± 0.02
5.20948 ± 0.00004	5.0	13.05 ± 0.08
5.21745 ± 0.00007	16 ± 6	13.05 ± 0.07
5.31593 ± 0.00006	46 ± 4	13.67 ± 0.03
5.31795 ± 0.00003	5.0	13.1 ± 0.1
5.31906 ± 0.00007	62 ± 4	13.88 ± 0.03
5.64574 ± 0.00003	6.5	13.2 ± 0.2
5.7354 ± 0.0002	36 ± 13	13.2 ± 0.1
5.76781 ± 0.00009	36 ± 6	13.31 ± 0.05
6.0996 ± 0.0001	39 ± 8	13.34 ± 0.06
<i>VDES J0224-4711</i>		
4.91166 ± 0.00003	28 ± 4	13.35 ± 0.05
4.9136 ± 0.0001	56 ± 20	13.1 ± 0.1
4.91529 ± 0.00003	19 ± 3	13.25 ± 0.04
4.99276 ± 0.00005	49 ± 5	13.37 ± 0.03
5.00508 ± 0.00003	32 ± 4	14.2 ± 0.1
5.0061 ± 0.0007	58 ± 21	13.7 ± 0.3
5.10894 ± 0.00003	58 ± 2	15.02 ± 0.04
5.11325 ± 0.00003	22 ± 2	14.23 ± 0.05
6.03082 ± 0.00005	16 ± 4	13.62 ± 0.07
6.17255 ± 0.00006	35 ± 4	13.98 ± 0.04
<i>PSO J036.5078+03.0498</i>		
4.99126 ± 0.00002	51 ± 1	14.39 ± 0.01
5.1488 ± 0.0001	61 ± 7	13.72 ± 0.05
5.2428 ± 0.0001	60 ± 7	13.95 ± 0.04
5.24474 ± 0.00006	22 ± 5	13.58 ± 0.07
5.6885 ± 0.0002	21 ± 13	13.2 ± 0.1
5.8121 ± 0.0001	43 ± 9	13.26 ± 0.07
5.8262 ± 0.0001	50 ± 8	13.44 ± 0.05
5.89869 ± 0.00004	9 ± 4	13.7 ± 0.1
5.90223 ± 0.00001	32 ± 8	13.2 ± 0.1

^a Combination of two lines closer than $\Delta v = 50$ km s $^{-1}$. See Section 2.1.

APPENDIX A: UPDATE ON THE $Z \sim 6$ C IV ABSORBERS

In this section, we report the lists of C IV lines with $\log N(\text{C IV}) \geq 13.0$, used in the present analysis from the three new spectra of quasars at $z \sim 6.5$ (see Section 2.3). A more thorough analysis of all the absorbers detected in those spectra is deferred to a further paper.